COMPUTATIONAL MODELING OF ISOTHERMAL FLOW PATTERNS: EFFECT OF SURFACE WETTABILITY AT DIFFERENT SCALES

Natan Padoin

Alan Z. de Souza

Cíntia Soares

natan.padoin@posgrad.ufsc.br

alanzago@hotmail.com

cintia.soares@ufsc.br

Departamento de Engenharia Química e Engenharia de Alimentos (EQA), Universidade Federal de Santa Catarina (UFSC)

Campus Reitor João David Ferreira Lima, 88040-900, Florianópolis, SC, Brasil

Abstract. *Surfaces can be classified as wettable or nonwettable, depending on the contact angle at the triple line among the gas-liquid-solid phases. While at the macroscale the surface to volume ratio is small and, thus, the influence of the bulk properties is significant, when microscale flow is considered the influence of the solid-fluid interface at the walls should not be neglected. In this scale, the contact angle may influence the flow pattern developed in the channel (e.g., stratified, slug, bubble, etc.), which, by its turn, exert strong influence on the pressure drop and the interfacial area available for heat and mass transfer, for instance. Therefore, the contact angle can be, at least indirectly, a key parameter in the design and analysis of these systems. Based on this scenario, the aim of this study was to apply commercial CFD packages to the evaluation of the effect of contact angle on multiphase flow at different scales. Experimental data was collected from the literature and used for the model validation. Moreover, an investigation of the effect of the numerical schemes and the dimensionless numbers controlling the physics was conducted.*

Keywords: *Numerical methods, CFD, Contact angle, Multi-scale.*

1 INTRODUCTION

In the modeling of multiphase flows, several parameters play a major role for precise description of the system under analysis, including the surface tension at the interface of the phases and the contact angle established among the phases and the walls. In fact, the computational simulation of these systems is considerably difficult and several numerical techniques have been proposed to account for the evolution of the topology of interfaces. Moreover, while the surface tension at the interface may be considered a scale-independent factor, since it always has a strong influence on the flow evolution, the contact angle is dependent on the scale of analysis, since at the macroscale the importance of the bulk properties are predominant, but at reduced scales the surface/volume ratio is considerably increased, giving rise to important interactions between the solid wall and the fluids.

Choi *et al.* (2011) demonstrated experimentally that the gas-liquid flow patterns developed in microchannels with different surface wettability were significantly different. Rectangular microchannels with average hydraulic diameter of ~500 μm were investigated and each phase, gas (nitrogen) and liquid (water), were fed at different inlets in a T-junction mixer. Chemical superficial treatment allowed the obtainment of hydrophilic and hydrophobic walls with contact angles of 25º and 125º, respectively. While the bubbly, elongated bubble and liquid ring flow patterns were observed in the hydrophilic microchannels, the non-lubricated elongated bubble, stratified and wavy stratified flow with entrainment were obtained in the device with hydrophobic walls. Therefore, it can be inferred that at the microscale the contact angle has strong influence on the system dynamics, once affecting the flow pattern it affects the pressure drop in the device, as well as the interfacial area available for heat and mass transfer among the *n* phases.

Based on this scenario, several computational strategies have been proposed for the numerical simulation of multiphase flow taking into account the influence of the wall adhesion. Fang *et al.* (2008) used the *Volume of Fluid* (VOF) method to simulate contact angle hysteresis in microscale isothermal two-phase flow. Schönfeld and Hardt (2009) and Deganello *et al.* (2011) investigated numerically the issue of dynamic contact angles. Yokoi *et al.* (2009) and Malgarinos *et al.* (2014) studied the role of contact angle in droplet spreading.

In fact, each of the models available has advantages and disadvantages when applied to different circumstances. A clear understanding of the model limitations is an important process in accurate modeling of any physical phenomenon. In this work, two distinct numerical schemes, the *Volume of Fluid* (VOF) and *Phase Field* (PF) methods, implemented in the commercial CFD codes ANSYS® Fluent® and COMSOL® Multiphysics®, respectively, were evaluated for the numerical simulation of droplet impact dynamics and the performance of both strategies was assessed. Further, a study at different scales was performed using the VOF method for the investigation of scale-effects on the development of gas-liquid flow patterns in channels. Finally, a study based on experimental data published in the literature was carried out to elucidate the effect of varying the contact angle on the gas-liquid flow regimes developed in microchannels. It should be highlighted that, although there are published works concerning the application of CFD codes to the investigation of the effect of contact angle in multiphase flow, there is lack of information about performance at different

scales and consequences of varying wettability on the development of multiphase flow regimes, which constitutes the main novelty of this paper.

2 METHOD

2.1 Numerical Approach

As mentioned in Section 1, in this work two different numerical schemes were applied to the calculations, namely the *Volume of Fluid* (VOF) and the *Phase Field* (PF) methods. In both cases the Navier-Stokes and continuity equations (Eq. (1) and Eq. (2), respectively) govern the flow inside the computational domain:

$$\rho\left(\frac{\partial \mathbf{u}}{\partial t}+\mathbf{u}\cdot\nabla\mathbf{u}\right)=-\nabla p+\nabla\cdot\left(\mu\left(\nabla\mathbf{u}+\nabla\mathbf{u}^{T}\right)\right)+IF+\rho\mathbf{g}, \tag{1}$$

where ρ (kg·m^{-3}) is the density, $\boldsymbol{u}$ (m·s^{-1}) is the velocity field, t (s) is time, p (Pa) is the pressure, μ (kg·m^{-1}·s^{-1}) is the dynamic viscosity and $\boldsymbol{g}$ (m·s^{-2}) is the gravity acceleration vector.

$$\nabla\mathbf{u}=0 \tag{2}$$

In this derivation incompressible flow is considered, which is a reasonable assumption in the cases studied. The function *IF* assumes different forms in COMSOL® Multiphysics® (Finite Element-based) and ANSYS® Fluent® (Finite Volume-based). In ANSYS® Fluent®, *IF* is represented by Eq. (3):

$$IF=\sigma\kappa\frac{\rho\nabla\alpha}{1/2\left(\rho_1+\rho_2\right)}, \tag{3}$$

where σ (kg·s^{-2}) is the surface tension coefficient, κ (m^{-1}) is the interface curvature, α (dimensionless) is the phase volume fraction, ρ (kg·m^{-3}) is the density and the subscripts (1, 2) indicate the phases.

In the VOF scheme the interface curvature (κ) is computed through the model of Brackbill *et al.* (1992). Using this method κ is calculated as the divergence of the unit vector normal to the interface, according to Eq. (4):

$$\kappa = \nabla \cdot \hat{n}, \tag{4}$$

where the vector normal to the interface and its unit correspondent are given by Eqs. (5) and (6), respectively (Fluent, 2013):

$$n = \nabla \alpha \tag{5}$$

$$\hat{n} = \frac{n}{|n|} \tag{6}$$

At the cells adjacent to the walls, the unit normal vector (Eq. 6) is modified by the specified contact angle, according to Eq. (7):

$$\hat{n} = \hat{n}_w \cos\theta_w + \hat{t}_w \sin\theta_w, \tag{7}$$

where $\hat{n}_w$ is the unit vector perpendicular to the wall, $\hat{t}_w$ is the unit vector tangential to the wall and θ_w is the specified contact angle. Values of $\theta_w < 90°$ represent a hydrophilic or wetting wall, while $\theta_w > 90°$ is used to describe a hydrophobic or non-wetting wall.

The physical properties (density and dynamic viscosity) are calculated through a mixing rule taking the phase volume fraction as weighting factor. Equation (8) presents the calculation procedure for the density and dynamic viscosity:

$$\begin{aligned} \rho &= \alpha_g \rho_g + \left(1-\alpha_g\right)\rho_l \\ \mu &= \alpha_g \mu_g + \left(1-\alpha_g\right)\mu_l \end{aligned} \tag{8}$$

Finally, it should be emphasized that in the VOF method the interface between the phases is tracked according to Eq. (9):

$$\frac{\partial \alpha}{\partial t} + \mathbf{u} \cdot \nabla \alpha = 0 \tag{9}$$

On the other hand, in the PF scheme the fluidic interface is computed through the Cahn-Hilliard equation (Eq. (10)):

$$\frac{\partial \phi}{\partial t} + \mathbf{u} \cdot \nabla \phi = \nabla \cdot \frac{\gamma \lambda}{\varepsilon^2} \nabla \psi, \tag{10}$$

where ϕ (dimensionless) is the phase field variable, $\boldsymbol{u}$ is the fluid velocity ($m \cdot s^{-1}$), γ is the mobility parameter ($m^3 \cdot s \cdot kg^{-1}$), which defines the time-scale of the Cahn-Hilliard equation, λ is the mixing energy density ($kg \cdot m \cdot s^{-2}$) and ε (m) is the interface thickness parameter. Additionally, the function ψ (phase field help variable) is defined according to Eq. (11):

$$\psi = -\nabla \cdot \varepsilon^2 \nabla \phi + \left(\phi^2 - 1\right)\phi + \left(\frac{\varepsilon^2}{\lambda}\right)\frac{\partial f_{ext}}{\partial \phi} \tag{11}$$

The volume fraction is computed according to the operation described in Eq. (12):

$$V_f = \min\left(\max\left(\left[\left(1+\phi\right)/2\right], 0\right), 1\right) \tag{12}$$

Furthermore, in the PF method the mean curvature κ can be computed according to Eq. (13):

$$\kappa = 2\left(1+\phi\right)\left(1-\phi\right)\frac{G}{\sigma}, \tag{13}$$

where G represents the chemical potential defined according to Eq. (14):

$$G = \lambda\left(-\nabla^2\phi + \frac{\phi\left(\phi-1\right)}{\varepsilon^2}\right) + \frac{\partial f}{\partial \phi} \tag{14}$$

2.2 Problem Setup

Initially, numerical simulations of droplet impact dynamics were carried out in the axisymmetric 2D domain presented in Fig. 1. A water droplet with initial diameter of 2.28 mm, according the study of Yokoi *et al.* (2009), was placed in an air rectangular enclosure (5 mm × 7.5 mm). As indicated in the scheme, the boundary conditions were specified as follows: axis of symmetry at the left boundary, ambient pressure (p = 0 Pa) at the top and right boundaries and, finally, a wetting wall at the bottom of the domain. This former boundary condition allowed the assignment of the contact angle. The same setup was

followed in COMSOL® Multiphysics® and ANSYS® Fluent®, with standard solver configurations.

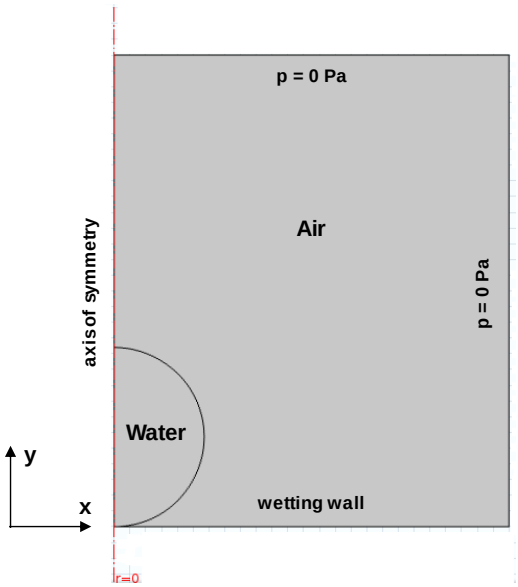

Figure 1: Computational domain and boundary conditions adopted in the numerical simulations of droplet impact dynamics.

All simulations were performed in the time domain, evolving from an initial state in which air (phase 1) was at rest, while an initial velocity of -1 $m \cdot s^{-1}$ along the y-axis was assigned to water (phase 2). Moreover, in all cases non-structured grids were used.

Further, an analysis at different scales was performed aiming to illustrate the influence of the scale of analysis on the morphological development of two-phase isothermal flow in horizontal ducts. The VOF method (ANSYS® Fluent®) was used in this study. Particularly, the second order interface reconstruction scheme PLIC (or geo-reconstruct in the context of the referred software) was applied.

Due to the symmetry of the geometries investigated, 2D computational domains were analyzed. For the simulation of multiphase flow in macroscopic device, a duct with length of 7 m and diameter of 8 cm was used, while a duct with length of 0.7 m and 0.8 cm of diameter represented the microscopic scale. For each scale evaluated, two different mass fluxes for the gas and liquid phases were assigned at the inlet boundary, resulting in the bubble and stratified flow patterns as predicted by the Baker chart (De Schepper *et al.*, 2008). This flow regime map allows the prediction of the two-phase flow arrangement in macroscopic equipment and was used as a criterion for the validation of the results obtained in the larger duct. In particular, mass fluxes of 10,000 $kg \cdot m^{-2} \cdot s^{-1}$ and 10 $kg \cdot m^{-2} \cdot s^{-1}$ were specified for the gas (air) and liquid (water) phases, respectively, for the development of bubble flow pattern, while the mass fluxes of 10 $kg \cdot m^{-2} \cdot s^{-1}$ and 1 $kg \cdot m^{-2} \cdot s^{-1}$ were assigned for the gas and liquid phases, respectively, for the stratified regime. At the outlet of the computational domains null gauge pressure was specified. Furthermore, the no-slip boundary condition was imposed at the upper and bottom walls. Additionally, a constant contact angle of 90° was considered at both walls. Gravity was taken into account in all simulations.

Constant physical properties were assigned for both fluids used in the simulations: density of 998.2 $kg{\cdot}m^{-3}$ and 1.225 $kg{\cdot}m^{-3}$ for the liquid and gas phases, respectively, and dynamic viscosity of 1.003×10^{-3} $kg{\cdot}m^{-1}{\cdot}s^{-1}$ and 1.789×10^{-5} $kg{\cdot}m^{-1}{\cdot}s^{-1}$ for water and air, respectively. In addition, a constant surface tension coefficient of 7.197×10^{-3} $kg{\cdot}s^{-2}$ was specified.

Mesh independence studies were performed and the optimized grids obtained for the macro and micro-scale ducts consisted of rectangular elements with edges of 2.5×10^{-3} m and 2.0×10^{-3} m, respectively. The Courant–Friedrichs–Lewy (CFL) condition was used as criterion for the definition of the time-step size (CFL = 0.25). Therefore, time-step sizes in the range of 10^{-3} s to 10^{-5} s were obtained. All simulations were performed until the statistical stationary state was reached (Milioli and Milioli, 2010), i.e., when the monitored velocity and pressure profiles throughout the channels did not present significant variation between two time intervals. Residuals below 1×10^{-3} were adopted as convergence criterion for all conservation equations or 80 iterations in each time-step, whichever was reached first.

The pressure-based solver was used. Moreover, the pressure-velocity coupling was treated in a segregated fashion with the SIMPLE algorithm. Gradients were evaluated through the least squares cell based technique. Additionally, the PRESTO and second order upwind schemes were applied to the spatial discretization of pressure and momentum, respectively. All sub-relaxation factors were maintained in their default values.

Furthermore, the effect of varying the wall contact angle on the developing two-phase flow pattern was investigated in a rectangular channel with microscopic dimensions. In particular, the same experimental setup adopted by Choi *et al.* (2011) was used in this work to validate the numerical simulations with the data obtained by those authors. In their work Choi *et al.* (2011) investigated the effect of the wall contact angle on the flow pattern developed in microchannels. Fig. 2 presents the numerical setup details.

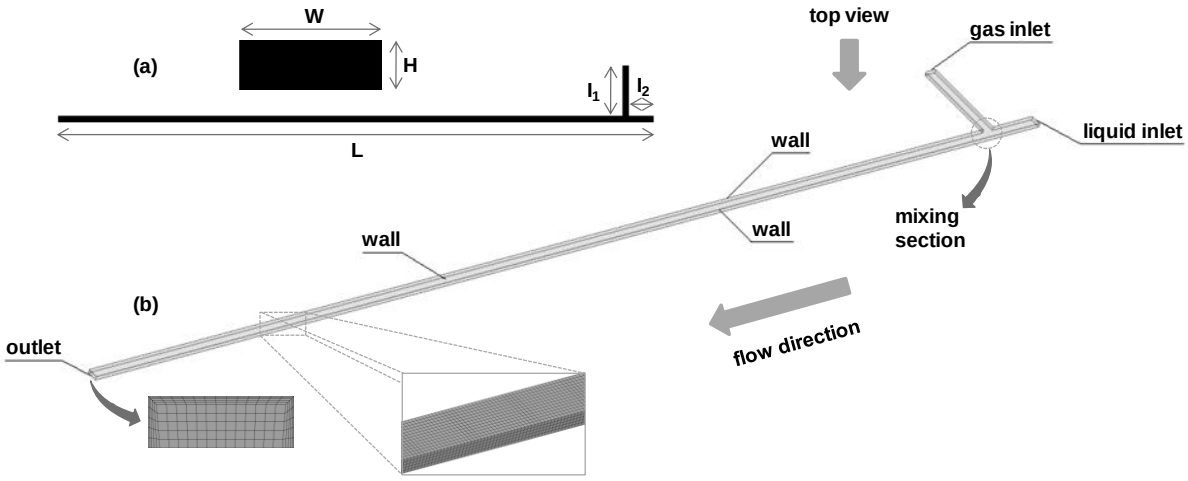

Figure 2: Computational domain used in the CFD simulations: (a) characteristic dimensions and (b) boundary conditions and mesh details.

In this study, a 3D computational domain was adopted. The main channel length (L) consisted of 57.5 mm. The gas and liquid streams were fed to the mixing section through

perpendicular channels with 5.0 mm (I_1) and 2.5 mm (I_2), respectively. The width and height of the channel (main and inlet sections) varied according to the wall wettability in order to comply with the experimental platform. Two scenarios were investigated: when the wall contact angle was maintained at $\theta = 25°$ the dimensions W and H were specified as 617 μm and 215 μm, respectively; on the other hand, when the wall contact angle was specified as $\theta = 105°$, W and H assumed the values 608 μm and 205 μm, respectively. Symmetry was assigned at the half-height of the domain.

Two different set of inlet velocities for the liquid (water) and gas (nitrogen) phases were studied in the channel with $\theta = 25°$ ($u_L = 0.43$ m·s^{-1} and $u_G = 0.07$ m·s^{-1}; $u_L = 0.19$ m·s^{-1} and $u_G = 0.32$ m·s^{-1}), while a single set of velocities was used in the duct with $\theta = 105°$: $u_L = 0.31$ m·s^{-1} and $u_G = 7.98$ m·s^{-1}. The no-slip boundary condition was applied at the channel walls. Additionally, null gauge pressure was specified at the outlet. The same numerical scheme previously reported (in the investigation of the scale effect) was used in this study. A mesh independence study was performed and quadrilateral elements with regular edge of 5.0×10^{-5} m were adopted.

3 RESULTS AND DISCUSSION

Initial studies of drop impact dynamics aimed to show the ability of the numerical schemes in capturing the morphological evolution of a water droplet falling on a wetting surface ($\theta = 90°$) with a velocity of 1 m·s^{-1} (along the y-axis). In particular, this study was based on the observations of Yokoi *et al.* (2009).

Using the *Phase Field* (PF) method in COMSOL® Multiphysics® allowed the reproduction, at least qualitatively, of the drop morphology along the entire time range evaluated. However, significant dependence on the mobility parameter (γ) and the grid refinement was noticed. The parameter γ controls the time-scale of the Chan-Hilliard equation and should be defined in an adequate range to maintain the interface thickness constant and avoid over-damping of the convective contribution. Fig. 3 presents the contours of volume fraction (red = air, blue = water) obtained from simulations with a grid composed by 21,193 elements and considering $\gamma = 0.3$.

It can be clearly seen that the droplet evolved from its initial spherical shape (at $t = 0$ s) until a nearly flat morphology was reached at $t = 4$ ms, from which a receding behavior was observed tending to a rest state at $t = 30$ ms. When compared with the experimental data obtained by Yokoi *et al.* (2009), the morphological profiles obtained present reasonable agreement, as evidenced in Fig. 4, which compares the experimental drop shape and revolution surfaces obtained from our 2D axisymmetric simulations.

The best agreement between the experimental and numerical results was observed in the advancing period (from $t = 0$ ms to $t = 4$ ms). In the receding phase (from $t = 10$ ms to $t = 30$ ms), however, the numerical predictions showed deviations from the experimental morphology, although the general qualitative behavior was reproduced. These observations are in line with the numerical results obtained by Yokoi *et al.* (2009) using the *Level-Set*/*Volume of Fluid* (LS-VOF) approach.

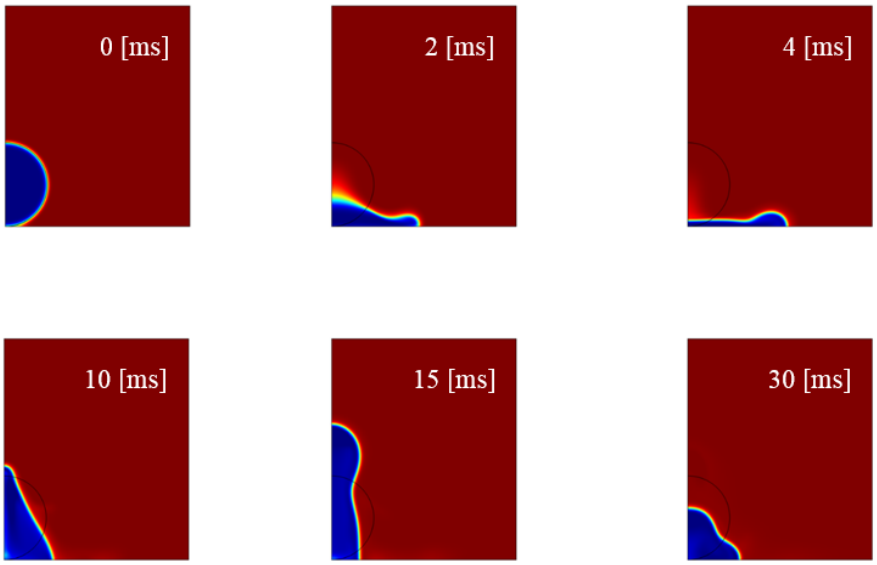

Figure 3: Contours of volume fraction obtained from the numerical simulations in COMSOL® Multiphysics® (PF method) with a grid composed by 21,193 elements and $\gamma = 0.3$.

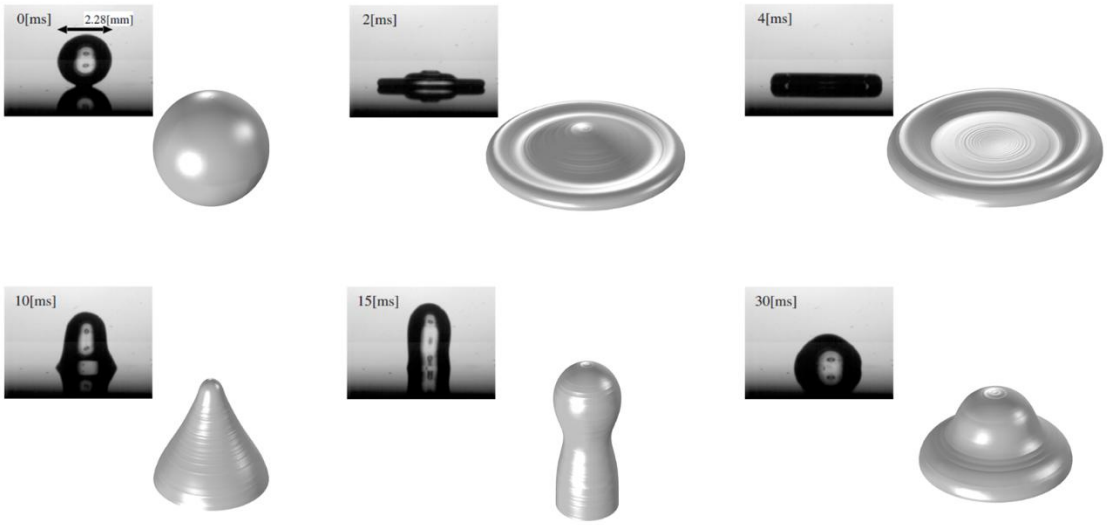

Figure 4: Revolution surfaces obtained from the numerical simulations in COMSOL® Multiphysics® (PF method) with a grid composed by 21,193 elements and $\gamma = 0.3$; comparison with the experimental data of Yokoi *et al.* (2009) for each time frame.

However, even though the PF method allowed the obtainment of good results, it is significantly sensible to the value assigned to the mobility parameter (γ) and the number of elements in the numerical grid. Figure 5 presents the contours of volume fraction obtained when the PF method was applied with a grid consisting of 21,193 elements (the same grid previously used), but with $\gamma = 1.0$. Although a behavior similar to that observed in Fig. 3 is verified until t = 4 ms, significant deviations appear after t = 10 ms, leading to a clear

departure from the experimental morphology at t = 30 ms, in which a breakup of the droplet is noticed. On the other hand, Fig. 6 presents the contours of volume fraction obtained for γ = 0.3 and a refined grid, composed by 80,415 elements. Again, good agreement with the experimental behavior was observed in the advancing phase (from t = 0 ms to t = 4 ms), but deviations are found in the receding phase, culminating in the droplet breakup at t = 30 ms.

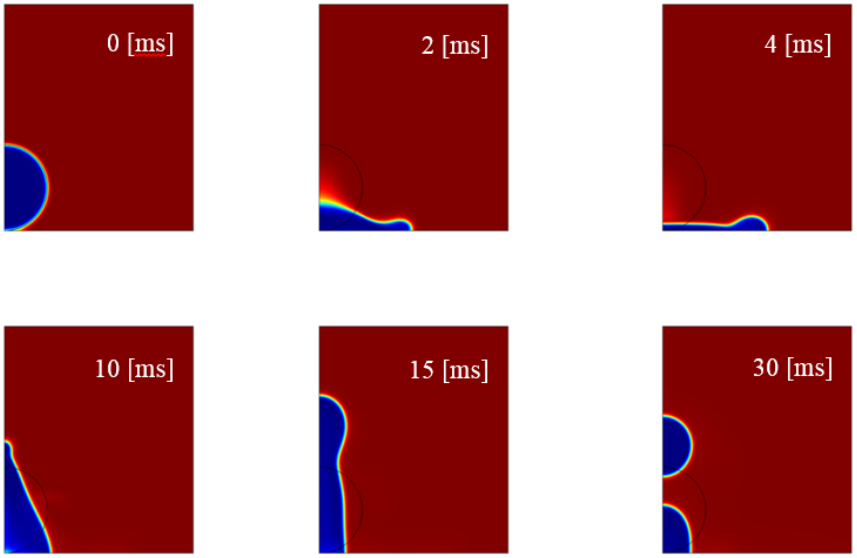

Figure 5: Contours of volume fraction obtained from the numerical simulations in COMSOL® Multiphysics® (PF method) with a grid composed by 21,193 elements and γ = 1.0.

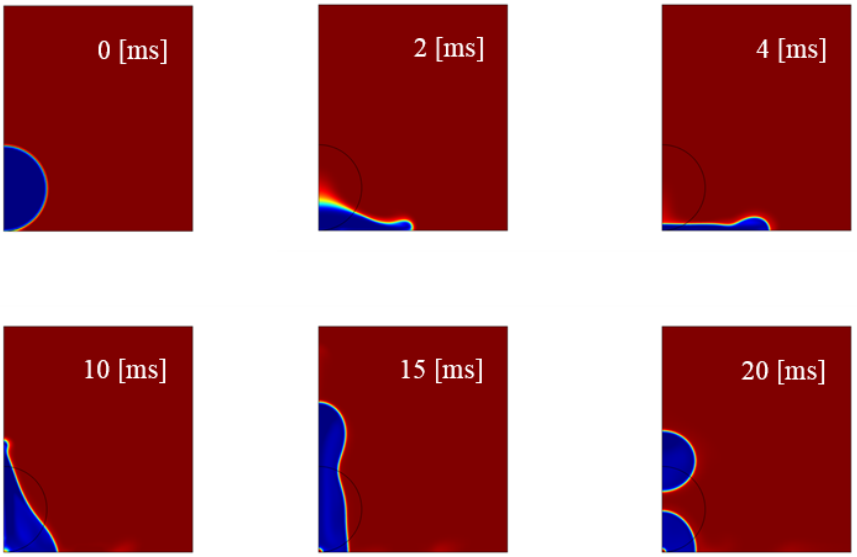

Figure 6: Contours of volume fraction obtained from the numerical simulations in COMSOL® Multiphysics® (PF method) with a grid composed by 80,415 elements and γ = 0.3.

In addition, it should be emphasized that poor mass conservation was observed in the simulations carried out with the PF method, as indicated in Fig. 7, which presents the average density in the computational domain along time. Moreover, it can be clearly seen that, for the same value of the mobility parameter γ, different grid refinements lead to similar behavior in the early phase of the numerical study (advancing period), but significant deviation was observed thereafter (receding phase). These observations are in line with those results reported in Figs. 3-6.

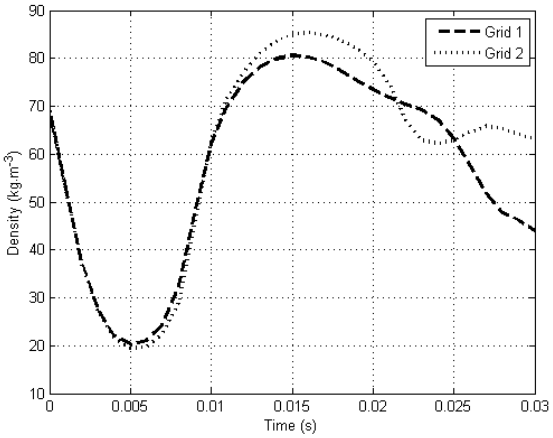

Figure 7: Average density in the computational domain along time. Grid 1 = 21,193 elements; Grid 2 = 80,415 elements.

In the computational simulations performed with the VOF method (using ANSYS® Fluent®) a different behavior was observed. Good agreement between the numerical results and the experimental data of Yokoi *et al.* (2009) was observed in the advancing phase (until t = 4 ms).

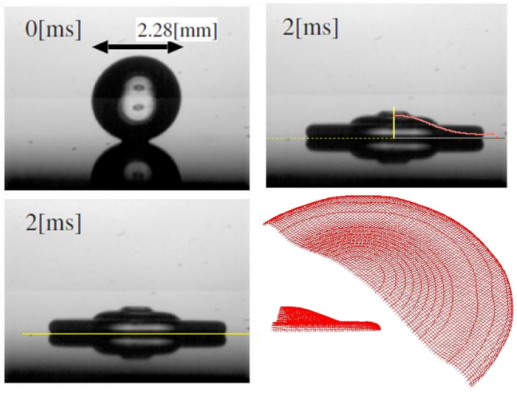

Figure 8: Comparison between the numerically obtained droplet morphology and the experimental data reported by Yokoi *et al.* (2009) at t = 2 ms with the VOF method. The initial droplet shape is showed for reference.

Figure 8 presents a comparison between the droplet morphology obtained numerically and the experimental shape photographed at t = 2 ms. However, differently from what was obtained when applying the PF method, the receding phase was not captured when using the VOF method. With this scheme the droplet continually spreads through the wetting surface from t = 0 ms until t = 30 ms. Therefore, at least from a qualitative point of view, the PF method performed better in reproducing the morphological evolution of a droplet impact dynamics, reconstructing both the advancing and the receding phases.

The VOF method was used for the evaluation of scale effect in ducts subjected to similar feeding conditions, based on the Baker chart guidelines. In this direction, Fig. 9 presents the bubble flow pattern obtained in the channel with macroscopic dimensions (length of 7 m and diameter of 8 cm). The liquid phase (water) is colored in red, while the gas phase (air) is colored in blue. Due to the significant difference between the phase densities and the gravitational acceleration, the liquid phase is concentrated in the lower region of the channel, allowing air to flow close to the superior wall.

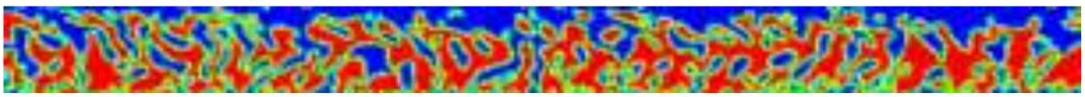

Figure 9: Contours of volume fraction obtained in the macroscopic duct (bubble flow pattern).

In line with the results previously presented, Fig. 10 present the stratified flow pattern obtained in the macroscopic duct. A well-defined and smooth interface separates the gas and liquid phases. These results validate the numerical study, since they corroborate the predictions of the Baker chart, used as source of information for the setup definition.

Figure 10: Contours of volume fraction obtained in the macroscopic duct (stratified flow pattern).

Based on the same inlet conditions specified for the bubble flow pattern in the macroscopic duct, Fig. 11 presents the contours of volume fraction (water in red and air in blue) for the microscopic duct. Even though a tenfold scale reduction was performed, the result agrees with the multiphase flow pattern predicted by the Baker chart for the feeding conditions applied. However, a clear distinction from the volume fraction profile obtained in Fig. 9 can be noticed.

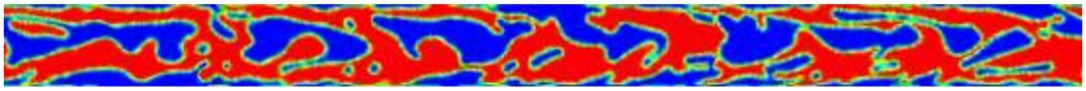

Figure 11: Contours of volume fraction obtained in the microscopic duct (bubble flow pattern).

Figure 12 presents the contours of volume fraction obtained for the same feeding conditions used in Fig. 10, but in the microscopic channel. In particular, Fig. 12a shows the entrance region of the duct, while Fig. 12b depicts an intermediary region of the channel. Differently from what was observed in the case of bubble flow pattern, the stratified regime did not hold when the duct scale was submitted to a tenfold reduction. In this scenario, it can be clearly seen that the liquid phase tended to a dispersed morphology, in which droplets with different sizes flowed grouped in the channel walls, while gas flowed in the center core.

Figure 12: Contours of volume fraction obtained in the microscopic duct (stratified-dispersed flow pattern).

As a general conclusion, it can be stated that as the channel dimensions are reduced from macroscopic length scales to a microscopic scale the relative importance of the wall on the flow is significantly higher and the bulk flow properties have diminished importance. Therefore, in microscopic devices the contact angle has a significant effect on the flow regime established, which impacts, by its turn, the area available for heat, mass and momentum transfer between the phases. Thus, the smaller the device the greater the importance of accurate modeling of contact angle applying adequate numerical methods.

Finally, Fig. 13 presents the results obtained in the investigation of the contact angle effect on two-phase flow patterns developed in microchannels, according to the experimental observations of Choi *et al.* (2011). In Fig. 13a-b the contact angle of $\theta = 25°$ was specified and, for both set of phase velocities assigned at the channel inlet, intermittent flow patterns (bubble and slug) were obtained. However, when the contact angle of $\theta = 105°$ was specified, stratified flow pattern was observed. Therefore, different contact angles can lead to different multiphase flow patterns for the same scale of analysis. Additionally, Fig. 13d-f presents comparisons between the numerical profiles and the experimental data obtained by Choi *et al.* (2011) and good agreement between them can be noticed.

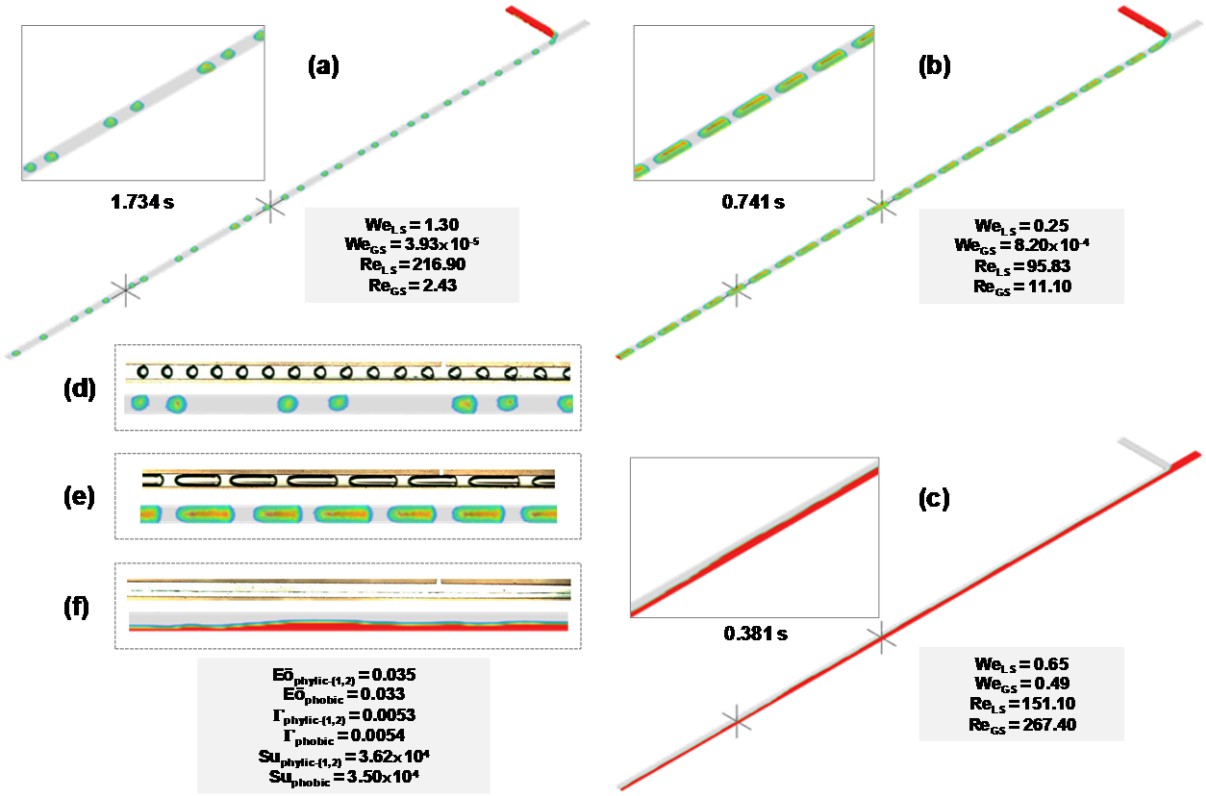

Figure 13: Three-dimensional flow patterns at the statistical steady state obtained for the cases (a, b) θ = 25° and (c) θ = 105°. Comparison between the top view of the experimental and numerically predicted flow patterns at the monitoring region for the cases (d, e) θ = 25° and (f) θ = 105°.

Attention should be paid to the fact that in all cases reported in Fig. 13 the Webber dimensionless number ($We = u^2 D_H \rho/\sigma$, where D_H is the hydraulic diameter) was smaller than the unity, indicating the higher importance of the surface tension forces when compared to inertial forces. Additionally, the low values of Reynolds dimensionless number ($Re = D_H u \rho/\mu$) in all cases indicate that laminar flow conditions was maintained even in case (c), when a relatively high gas velocity was assigned at the microchannel inlet.

4 CONCLUSIONS

The *Volume of Fluid* (VOF) and *Phase Field* (PF) methods presented limitations in the computational simulation of droplet impact dynamics: the PF method was able to capture both the advancing and receding phases, but showed significant dependence on the mobility parameter (γ) and the grid refinement; additionally, poor mass conservation was observed; on the other hand, the VOF method was able to capture the advancing phase with acceptable precision, but could not capture the receding phase.

Isothermal gas-liquid flow modeling (with VOF method) in horizontal channels revealed that significant deviations of the flow regime can occur when different scales are simulated. In particular, as the dimensions are reduced to microscopic scales there are increased importance of wall effects, including higher influence of the contact angle. Moreover, varying the wall wettability in microchannels can result in different gas-liquid flow patterns, which influence the interfacial area available for heat, mass and momentum transfer between the phases and, therefore, directly affects the performance of the system.

ACKNOWLEDGEMENTS

N. Padoin acknowledge CNPq for the PhD scholarship (process number 140521/2014-3). A. Z. de Souza acknowledge the program PIBIC UFSC/CNPq for the scholarship.

REFERENCES

Brackbill, J.U., Kothe, D.B., Zemach, C., 1992. A continuum method for modeling surface tension. *Journal of Computational Physics*, v. 100, n. 1, pp. 335-354.

Choi, C., Yu, D.I., Kim, M., 2011. Surface wettability effect on flow pattern and pressure drop in adiabatic two-phase flows in rectangular microchannels with T-junction mixer. *Experimental Thermal and Fluid Science*, vol. 35, n. 1, pp. 1086-1096.

Deganello, D., Croft, T.N., Willians, A.J., Lubansky, A.S., Gethin, D.T., Claypole, T.C., 2011. Numerical simulation of dynamic contact angle using a force based formulation. *Journal of Non-Newtonian Fluid Mechanics*, v. 166, n. 1, pp. 900–907.

De Schepper, S.C.K., Heynderickx, G.J., Marin, G.B., 2008. CFD modeling of all gas-liquid and vapor-liquid flow regimes predicted by the Baker chart. *Chemical Engineering Journal*, v. 138, n. 1, pp. 349-357.

Fang, C., Hidrovo, C., Wang, F., Eaton, J., Goodson, K., 2008. 3-D numerical simulation of contact angle hysteresis for microscale two phase flow. *International Journal of Multiphase Flow*, v. 34, n. 1, pp. 690–705.

Fluent, A., 2013. 15.0 Documentation. Ansys Inc.

Malgarinos, I., Nikolopoulos, N., Marengo, M., Antonini, C., Gavaises, M., 2014. VOF simulations of the contact angle dynamics during the drop spreading: Standard models and a new wetting force model. *Advances in Colloid and Interface Science*, v. 212, n. 1, pp. 1–20.

Milioli, C.C., Milioli, F.E., 2010. On the accuracy of two-fluid model predictions for a particular gas–solid riser flow. *Applied Mathematical Modelling*, v. 34, n. 1, pp. 684-696.

Schönfeld, F., Hardt, S., 2009. Dynamic contact angles in CFD simulations. *Computers & Fluids*, v. 38, n. 1, pp. 757–764.

Yokoi, K., Vadillo, D., Hinch, J., Hutchings, I., 2009. Numerical studies of the influence of the dynamic contact angle on a droplet impacting on a dry surface. *Physics of Fluids*, v. 21, n. 1, pp. 1–12.